Enabling Mars Exploration Using inflatable Purdue Aerodynamic Decelerator with Deployable Entry Systems (iPADDLES) Technology

Michael Sparapany*, Thomas Antony*, Harish Saranathan*, Lorenz Klug†, Ben Libben†, Eiji Shibata†, and Joseph Williams†

Advisors: Professor Michael Grant‡ and Professor Sarag Saikia§

Purdue University, West Lafayette, IN 47906
United States

*PhD Student, School of Aeronautics and Astronautics
†Masters Candidate, School of Aeronautics and Astronautics
‡Assistant Professor of Aeronautics and Astronautics
§Visiting Professor of Aeronautics and Astronautics

I. Background on Mars EDL Systems

The Entry, Descent, and Landing (EDL) phase of a Mars mission is one of the main challenges to overcome to make a human-class mission possible. The Martian atmosphere is dense enough to create concerns for heating, while not dense enough to provide sufficient drag to decelerate a high mass entry vehicle using traditional designs.[1] The recent Mars Curiosity rover mission, which landed one metric ton on Mars, possibly represents the limit of the current state-of-the-art technology using rigid aeroshells and supersonic parachutes. A new paradigm of entry vehicle design is required to overcome the challenge of landing heavier payloads on Mars. Hypersonic Inflatable Aerodynamic Decelerator (HIAD) technology is a leading candidate for building large aeroshells which is expected to be capable of delivering masses of 15 to 30 metric tons safely to the surface of Mars.

Aerodynamic lift is crucial for such entry vehicles to ensure pinpoint landing and to reduce stresses on the vehicle and its payload. Current HIAD concepts rely on flying an axisymmetric HIAD at an angle-of-attack (AoA) (using center-of-gravity shift or control surfaces) to generate lift. In this technical paper, a shape-morphing design is presented that is based on the existing stacked-toroid HIAD concept. One of the major benefits of a HIAD is that it can be stowed for launch and deployed to very large diameters later. This benefit can be retained in this design by using deployable, inflatable flaps that can be stowed during launch.

Design simplicity, overall system mass, and aerodynamic characteristics are taken into account throughout this analysis. The developed technology should be extensible to aeroshell diameters between 15 and 20 meters, as well as generate modulated lift to drag ratio from 0.20 to 0.50. The design needs to possess a smooth outer mold line to prevent localized heating and be aerodynamically stable throughout the hypersonic flight phase.

II. Literature Review

An extensive literature review was done on HIADs, both static and morphing. Smith et al. describes a variety of Inflatable Aerodynamic Decelerators (IADs), and the advantages and disadvantages of both trailing and attached IADs.[2] Their conclusions state that an attached configuration is more drag and mass efficient, and that a tension cone design creates an attached shock at the back of the aeroshell, producing significant heating. This led the team to settle on an attached stacked toroid configuration for the base design.

Multiple NASA missions have flown this design, one of which flew with a center of gravity (CG) shift to create a lifting entry vehicle. Dillman explained the performance of NASA's second Inflatable Reentry Vehicle Experiment (IRVE), which demonstrated the stability and aerodynamic performance of a ballistic stacked toroid IAD, as well as its deployment.[3] IRVE-III, according to Dillman et al., was aimed at demonstrating the effectiveness of a CG offset on the Lift to Drag ratio (L/D) of a stacked toroid IAD.[4] They illustrated that the stacked toroid configuration with an L/D of 0.17 acted as a rigid body, showing the aeroelastic stability of the design.[5]

As IRVE II and III had a 3 m diameter, assessing the scalability of the stacked toroid design were done with NASA's High Energy Atmospheric Reentry Test (HEART) and LDSD (Low Density Supersonic Decelerator).[6] According to Wright et al. HEART's size and atmospheric test environment is consistent with robotic planetary missions to Mars.[7] Wright and Cheatwood explained that HEART will demonstrate the readiness of HIADs for mission infusion, and they currently have a 6 m diameter test article.[7] LDSD's successful flights demonstrated the ability to manufacture and fly an IAD with a diameter of around 20 ft.

Harper and Braun looked into asymmetrical HIADs and compared the effectiveness of biconics, flat, and shifted bodies.[8] While they found that these asymmetric HIADs can achieve a low trim angle and constant L/D of around 0.3, the flat and biconic designs show a decrease in their drag coefficient when increasing their lift due to the reduction in reference area compared to a symmetrical body. The shifted design did show promising results for L/D increase alongside an increase in drag, but had poor stability at high shifted percentages.

Green looked into dynamic morphing HIAD shapes, and optimized the shapes for heating and L/D using superellipses.[9] Green proposed to achieve his optimized shape by starting with a symmetric HIAD, and morphing it using a system of cables, pulleys, and a rotary motor to pull the sides in. While his design is simple in theory, the system introduced too many single point failures, as well as introducing a lot of added mass. Our team chose our proposed design keeping these considerations in mind.

III. Design

We propose a stacked inflatable toroid structure that is covered by an flexible thermal protection system (TPS) cloth. The payload is located within the center of the toroids and placed near the heat shield, which maintains a forward CG. To enable static stability, several inflatable flaps are placed near the aft.

Inflatable flaps make it possible to present a variety of vehicle shapes to the oncoming flow. Retracted, the vehicle forms an axisymmetric sphere-cone flying at zero AoA producing no lift. Independently operating flaps are pushed into and out of the flow to create locally increased drag. Positioning them to maximize the distance from the CG ensures the moment applied to the spacecraft is also maximized. These moments cause the spacecraft to trim at a non-zero AoA and sideslip, which generates the controllability required for guidance.

An inflation system to morph the shape was looked into, but the complexity, mass, and volume of a system that can repeatedly inflate led to the idea to be discarded, as explained in Appendix F. The inflatable nature of the flaps also distributes some of the pressure force to the toroid, resulting in a lower force requirement from the actuators.

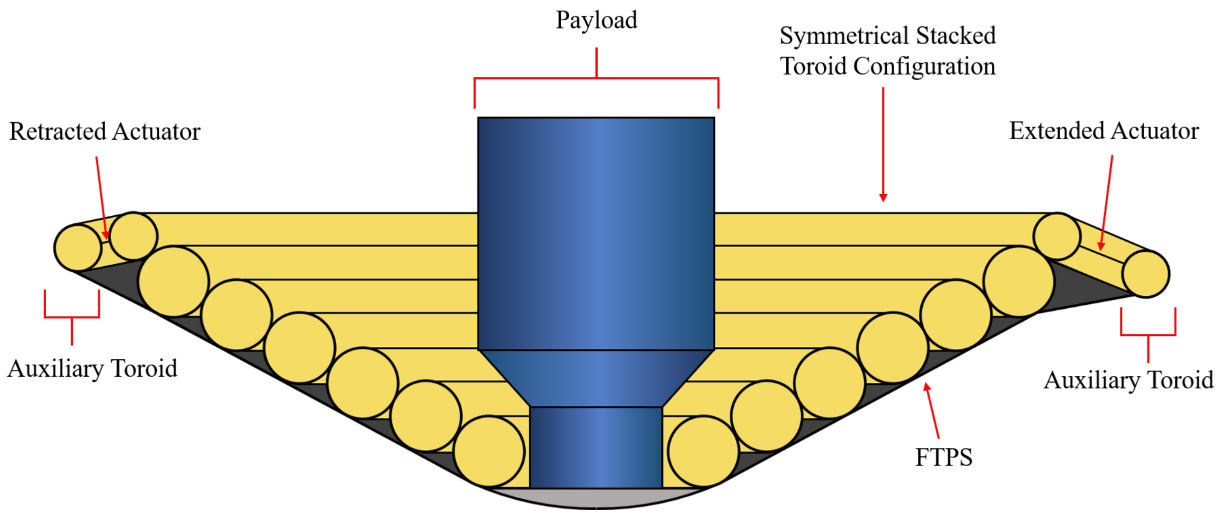

Figure 1: Side profile view of the proposed HIAD design.

IV. Concept Selection

The detailed design involved investigating variations of the aforementioned flaps. The variable architectures studied were the number of flaps, their location, radial length of the flaps, and arc length. The trade study evaluated L/D in each discrete design. Each iteration considered whether or not a trim condition and an L/D of 0.5 or larger was present with a flap configuration with angles of attack or sideslip $\pm 40°$.

For the arc length, there was a trade-off present between the mass of each flap and the amount of force each flap can place on the vehicle. However, it was seen that in order to minimize the moment that the actuators have to overcome from the oncoming flow, the radial length must be minimized. This forced the arc length to be maximized so that the area can be large enough to give an L/D of 0.5 or greater. Therefore, it was determined that the arc length would be the entire circle divided by the number of flaps. The overall radius was constrained to 10 m, making the flap radial distance and the main body radius variable. Therefore, to minimize the system mass and the required actuator force down, the radius was stepped up until an L/D of 0.5 was attained.

V. Aerodynamics and Control Authority

The aerodynamic properties are studied by employing Newtonian impact theory. In Newtonian flow theory, the fluid is assumed to transfer all of its normal momentum to the surface of the vehicle and retain all of its tangential momentum. A detailed analysis of the aerodynamics, flaps, and the resulting dynamical effects on the selected configuration of iPADDLES can be seen in App. B.

VI. Guidance Algorithm and Reference Trajectory Design

A. Side Slip Augmented Apollo Guidance

Since the expected mission objective is to target specific locations of scientific interest on Mars, the vehicle requires a guidance system that will enable it to achieve precision targeting. As a result, a new guidance algorithm named Sideslip Augmented Apollo Guidance (SAAG), derived from the flight-proven Apollo guidance algorithm, is proposed. Apollo guidance is rated for crewed vehicles and has been successfully implemented in the Apollo and Mars Science Laboratory (MSL) missions.

The Apollo guidance algorithm was altered to account for the different control characteristics of the iPADDLES vehicle design. The original algorithm[10] has the vehicle flying at a constant AoA, α_{Apollo}, which is between the body-fixed x axis ($\hat{x}_{Body}$) and wind frame x axis (x_{Wind}). The vehicle maneuvers by performing a bank angle (σ_{Apollo}), which is a rotation about the velocity vector (aligned with $\hat{x}_W$). This is illustrated in Fig. 2. Since α_{Apollo} is held constant, the drag coefficient also remains fairly constant throughout the hypersonic phase. As a result, the downrange and crossrange channels of the guidance algorithm can be decoupled, allowing the downrange channel to work with planar flight dynamics equations. The downrange channel determines the lift component along $-\hat{z}_W$, and the corresponding bank angle, required to target the desired final downrange. The crossrange channel determines the direction of the bank angle based on cross range error. It commands a roll reversal whenever the crossrange error hits a specified deadband.

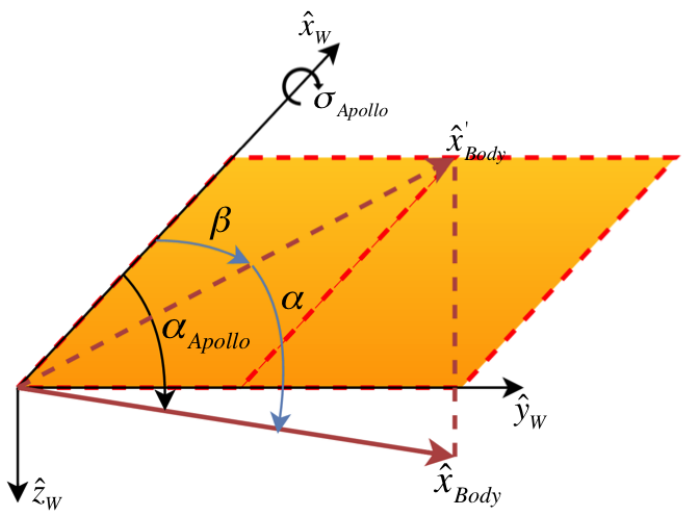

Figure 2: Illustration of resolution of bank-angle into AoA and side-slip sequence

Apollo and MSL performed bank maneuvers using reaction control system thrusters. Since the HIAD vehicle is controlled by deflecting tabs not capable of generating a roll moment, it does not have the capability to bank. However, since the vehicle remains largely axisymmetric, the same aerodynamic force vector can be attained by pointing $\hat{x}_{Body}$ in the same direction that would result from performing a bank maneuver. This can be achieved by introducing a sideslip (β) and a new AoA (α), as shown in Figure 2, by suitably deploying the tabs. α is the angle between $\hat{x}_{Body}$ and wind frame's $x-y$ plane. In essence, the commanded bank angle from Apollo guidance algorithm can be resolved into $\alpha - \beta$ sequence, and the tabs will be suitably deployed to trim the vehicle at those values.

Deploying the tabs will make the vehicle asymmetric. This results in variations in drag coefficient, violating the assumption of Apollo guidance algorithm. As a result, a correction coefficient was added to the sensed drag acceleration utilized by the downrange channel of the guidance algorithm, as explained in Appendix C.

The crossrange channel of the guidance algorithm was modified to command a roll reversal whenever the heading error hits a deadband, instead of the crossrange error used in the original algorithm. This resulted in better targeting, as observed from Monte Carlo analysis, explained in Section B. The crossrange channel of the guidance algorithm is explained in Appendix D.

Although the actual roll angle is not critical to the guidance performance, it is desirable to maintain zero roll rate. Since the tabs are not capable of generating any roll moment, a system needs to be developed to cancel any roll rate induced by environmental disturbances. Since such disturbances along the roll axis are expected to be small, one of the proposed solutions is to add reaction control thrusters to the roll axis.

B. Trajectory

Table 1: Initial and Terminal Conditions for the Reference Trajectory

State Variable	Initial Condition	Terminal Condition
Altitude	120 km	18.24 km
Longitude	0°.	18.59°.
Latitude	0°.	0°.
Velocity	6 km/s	600 m/s
Flight Path Angle	-13°.	-16.16°.
Heading	East	East

The initial and terminal conditions of the reference trajectory used to test the guidance algorithm are shown in Table 1. The trajectory is split into two phases, as illustrated in the schematic in Figure 3. The first phase is flown with a full lift up configuration until the flight path angle shallows out to almost level flight. This helps to reduce the peak g-loading, which is a critical parameter for human class missions. Once the flight path angle shallows out to $-0.5°$, the second phase of the trajectory begins, where the nominal bank angle profile is a constant 60°. In this phase, SAAG guides the vehicle to the desired target. Along this reference trajectory, peak heat rate and peak g-load are 28 W/cm^2 and 10 g, respectively. Heating will be further discussed in Section E. Without performing trajectory optimization, the g-loading can be reduced by simply making the entry flight path angle shallower. However, Monte Carlo analysis showed that with atmospheric dispersions, some trajectories skipped the atmosphere at hyperbolic speeds. As a result, the initial flight path angle was chosen to be $-13°$.

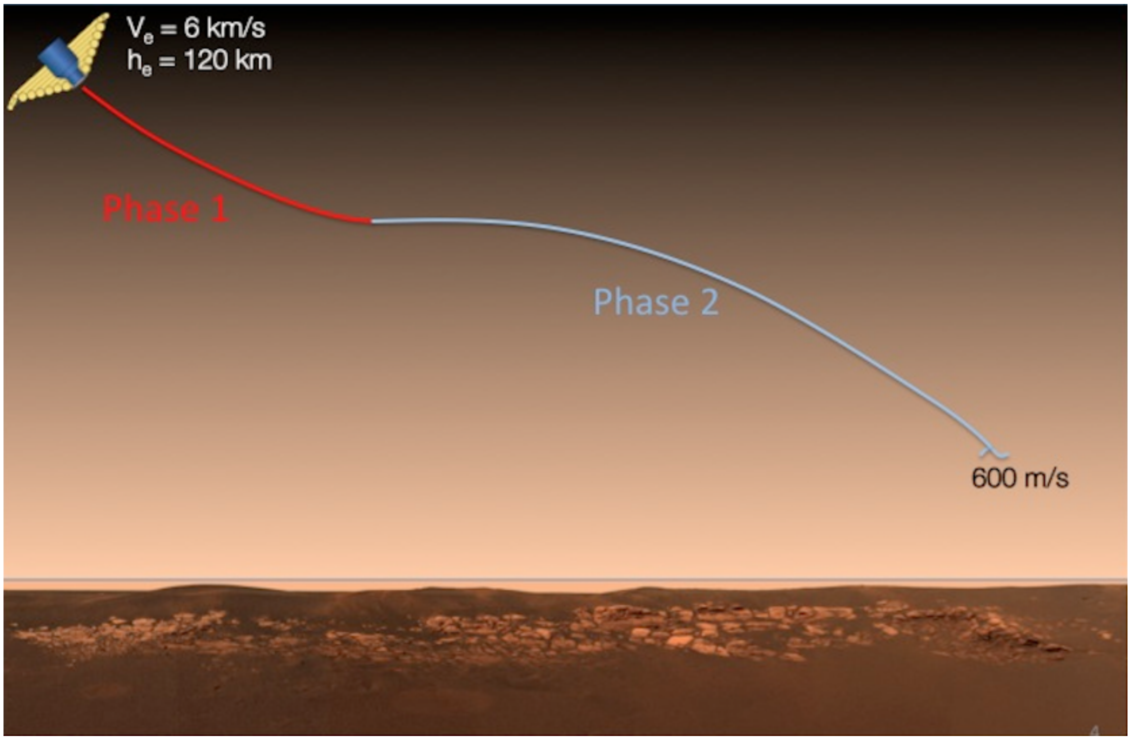

Figure 3: Illustration of reference trajectory

VII. System Sizing and Design

A. Actuator System Design

The proposed actuator subsystem is based off the ESA's Intermediate Experimental Vehicle (IXV) design, with a linear actuator pushing a pinned lever to extend the auxiliary toroid into the flow as shown in Figs. 4 and 5. Since the tabs only need to deflect 15° out into the flow with respect to the half cone angle to achieve an L/D of 0.5, the actuator only needs to extend about 0.2 m. A survey of existing actuators has shown that a stroke length of 0.2 m with an exerted force of about 110.9 kN is feasible with the weight of each actuator on the order of 10 kg.[11] In order to reduce single point failures, we propose to have three actuators on each flap, with each actuator being able to take about 54% of the peak dynamic pressure experienced. This gives redundancy to a previous system that has a single-point failure. If an actuator fails on each tab, the mission will not fail, creating a redundant system with only reducing approximately 0.4% of the payload mass.

The decision to use Electro-Mechanical Actuation (EMA) over hydraulic actuators stems from the increased accuracy and reliability, and the risks associated with hydraulics fluid freezing in transit. The EMA and lever arm system[12] utilized by the IXV and derived from the Vega Launcher boasts an operation range limit of -19° to 21° and an operation rate limit of 15 deg/s.[13] On the Vega Launcher two EMA/lever arm systems directed the nozzle for thrust vectoring while operating under 600 kN transient side loads.

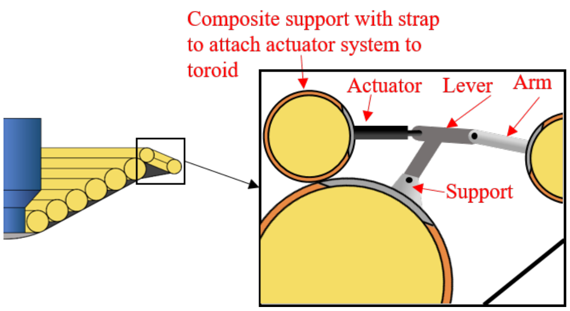

Figure 4: Side view of the actuator system. The actuator is attached to the small upper toroid by bolting it to a composite surface which is wrapped around the toroid with a strap.

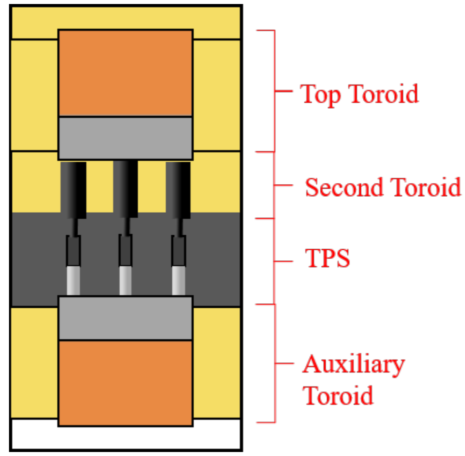

Figure 5: Top-down view of the actuator system. The actuator pushes the lever along the horizontal axis, pivoting about the support rod.

B. Actuator System Sizing

The flap size on the IXV had an approximate area of 0.3 m^2, while the area on the proposed HIAD design is 30.75 m^2. The difference in size is significant but due to the thinner Martian atmosphere the forces on the flaps are manageable.

A free body diagram analysis was performed on the system to determine the forces on each flap and for the sizing of the linear actuator. Assumptions applied to the analysis include: x-axis loading actuator, y-axis loading support beam, inflatable bodies act as wall supports, and each piece of the actuator system is a solid body. To determine the maximum loading on the actuator, the largest dynamic pressure along the trajectory was applied to the area of the flap. A factor of safety of 1.5 was applied to the resultant aerodynamic force on the system.

The actuator is predicted to encounter the strongest load when the flap is in the nominal position (in-line with the 70° cone angle) while the support beam had the largest load when the flap is extended into the flow due to the greater dynamic pressure tangent to the flow.

C. HIAD Sizing

Inflation pressures of the toroids are determined through comparing the Mach numbers and dynamic pressures experienced by the IRVE-2 and 3 system. IRVE-2 experienced a peak

Mach and dynamic pressure of 6.2 and 1,180 Pa, respectively,[14,15] while IRVE-3 experienced a peak Mach and dynamic pressure of 10 and 5,053 Pa, respectively. IRVE-2 utilized inflation pressures of 1.5 psig and IRVE 3 used 10 psig. The designed trajectory resulted in a peak dynamic pressure of around 4,400 Pa and Mach of 7. Using these examples as guideposts, an inflation pressure of 6 psig is selected. Additionally, IRVE-3 carried the inflation gas, nitrogen, in a 3,000 psi tank. Following this example, the same is planned for iPADDLES.

D. Payload Distribution

Mass distribution is important to keep the center of gravity as far forward as possible. To address this, the inflation system sits at the forward section, as opposed to the aft, due to its relatively high mass and to reduce overall complexity. Since the actuators require a heavy power source to operate, we propose to carry the power system in the payload, and run wires from the payload to the actuator systems. This design allows the mass to stay central and far forward. The rest of the electronics, the telemetry module, and interplanetary Attitude Control System (ACS) are placed on top of the power system, with the payload in the top-most portion.

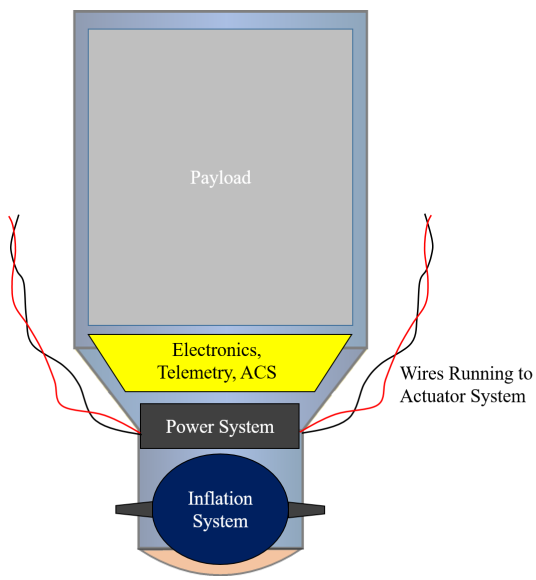

Figure 6: Cut-away view of the payload distribution to keep the CG as close to the nose as possible. The power system for the actuators are kept in the payload, and power is fed through the interior of the HIAD.

E. Thermal Protection System (TPS) Sizing

The flexible TPS cloth must withstand both the heating and the aerodynamic forces induced on the vehicle. Convective heat rate at the stagnation point experienced by the vehicle during entry is calculated using Sutton and Graves equation shown in Eq. 1.[16]

$$\dot{q}_s = k\sqrt{\frac{\rho}{r_n}}V^3 \tag{1}$$

Dynamic pressure and heat rate are then used to select the TPS material. Heat load is used for the sizing of the TPS thickness. As seen in Appendix E, the maximum heat rate is 28 W/cm^2. Additionally, the calculated heat load, J, is 1558 J/cm^2. These values are quite mild in comparison to past Mars missions such as Mars Pathfinder with an estimated peak convective stagnation-point heat rate of around 106 W/cm^2 and a total heat load of 3865 J/cm^2.[17] Note, the reference trajectory was created without considering heating. Therefore, through optimization it is possible further reduce the heat rate and heat load to fly the mission without the need of ablative TPS.

VIII. Overall System Feasibility

A. HIAD System Feasibility

An important consideration in the design of the morphing HIAD is whether or not it is feasible to produce. From previously flown NASA missions such as IRVE and HEART, it has been shown that a stacked toroid configuration can be manufactured and flown. The IRVE flight vehicles were both 3 meters in diameter however, an order of magnitude smaller than the design we are proposing. Despite this, HIAD technology is developing rapidly, with IRVE-4 and HEART-2 planned to demonstrate active control of a lifting body HIAD,[18] and HEART planned to demonstrate scalability with a current 6 meter diameter test article, and a planned 8 meter diameter flight test vehicle. The continued success of the IRVE program gives the stacked toroid design legacy. However, precedent does not exist for the linearly actuated control tabs on the HIAD.

B. Actuator-Flap System Feasibility

We are expanding on the heritage HIAD designs with a simple, yet robust, EMA system. Looking at previous missions from both the ESA and NASA, there are examples of actuated control surfaces. The X-38 used EMAs to adjust the vehicle's flight control surfaces for pitch, yaw, and roll control.[19] According to Gibbs, those same actuators were also used on previous NASA, Air Force, and Navy research projects. IXV used a similar design as the X-38, with linearly actuated control surfaces used to guide the space-plane's descent.

The next step in measuring the feasibility of the actuator subsystem was designing the attachment of the actuator subsystem to the base HIAD. Holes should not be punctured into the toroids to screw the actuator and lever arm into the HIAD, since that would increase deflation risk. Instead, we propose to attach the actuator subsystem to three composite cylindrical sections that have straps that wrap around the toroid as displayed in Figs. 4 and 5. This minimizes the weight added to the system and increases the packagability since the amount of rigid mass added is relatively small.

C. Packaging Feasibility

Referencing IRVE-3's packaging design, the HIAD will be packaged deflated at the front of the payload, with the top toroid being farthest from the payload.[4] The actuator system will be folded into a rectangular volume at the end of the fairing. The actuator subsystem folding can be seen in Fig. 7. The volume of the packaged HIAD is computed as just the surface area of the toroids multiplied by their thickness, and the packaged actuator system is an approximated rectangular volume based on the height, length, and width of each individual subsystem.

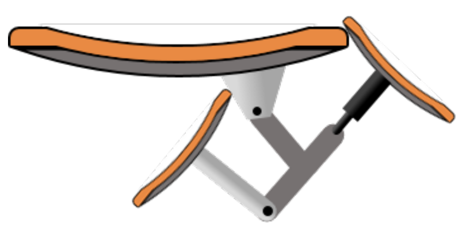

Figure 7: Side view of the packaged actuator system. When the toroids are deflated for packaging, the toroid attached to the linear actuator will sit slightly behind the large toroid ring, and the actuation system is folded into a smaller volume.

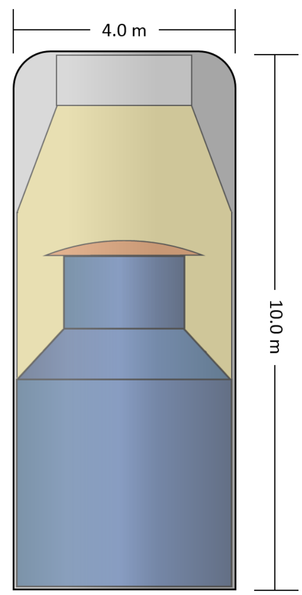

Figure 8: Cut away view of the payload fairing. The blue geometry is the payload, the yellow is the packed HIAD approximate volume, and the gray box is the approximate packaged actuator system volume.

D. System Feasibility

Since each individual system (stacked toroid HIAD and EMA system) have been demonstrated in flight, it can be concluded that they can each be manufactured. The main challenge comes with integrating the two systems together into a unified system. More analysis has to be conducted on the structural integrity of the HIAD-Actuator interface, and the stability of the connection needs to be looked into more closely in order to accurately determine the overall system's feasibility.

IX. Results from Analysis

A. Aerodynamics

The configuration in Fig. 9 shows the vehicle in a configuration such that it trims at an AoA of 30.9° and no sideslip angle. Figure 10 shows the plot of pitching moment coefficient as a function of AoA. This means that the vehicle can trim up to 30.9° AoA depending on the level of deployment of the flaps. The plot in Fig. 10 shows that the vehicle is statically stable.

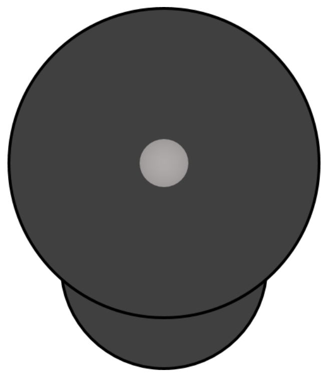

Figure 9: Front-on view of the HIAD in Maximum L/D Configuration. This particular configuration allows for a large amount of lift, while minimizing the drag from other flaps.

Fig. 11 shows the plot of lift-to-drag ratio as a function of AoA. At the maximum trim AoA (when one of the four flaps are fully deployed as shown in Fig. 1), the lift-to-drag ratio is approximately 0.5.

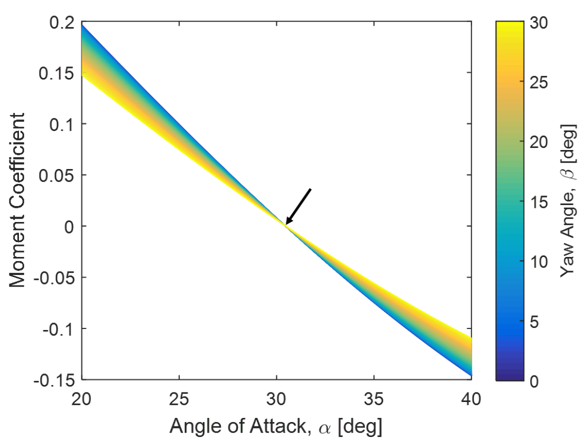

Figure 10: Pitching moment coefficient as a function of AoA. This flap configuration has a trim condition at approximately 31°.

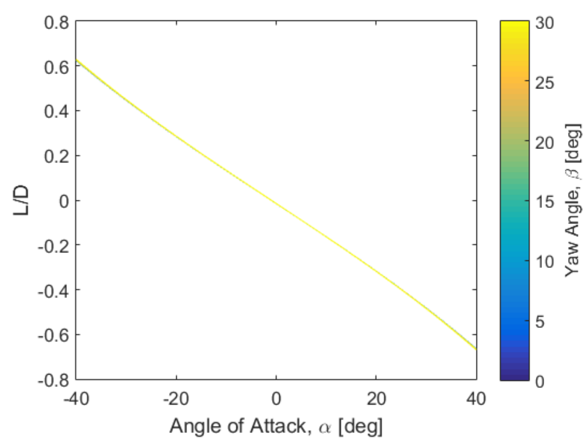

Figure 11: Lift-to-drag ratio as a function of AoA. For the corresponding trim AoA, the L/D is approximately 0.5.

Figure 12 represents the ballistic coefficient as a function of AoA, assuming a mass of

30,000 kg. At the trim AoA, the ballistic coefficient is 103 kg/m^2, which is less than MSLs 140 kg/m^2.[20] This shows that the chosen vehicle design can generate high drag while maintaining high lift-to-drag ratio. Other graphs corresponding to this flap configuration are located in App. B.A.

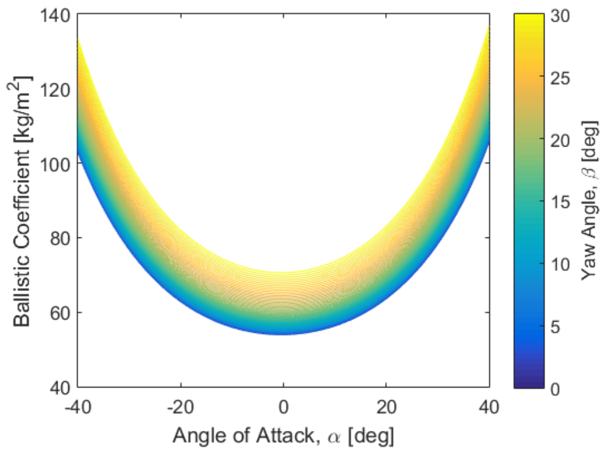

Figure 12: Ballistic coefficient as a function of AoA. As the vehicle does have trim conditions that have nonzero angles, there are a range of drag coefficients that are realizable. As such, this causes the ballistic coefficient to vary.

B. Monte-Carlo Simulation with Guidance

A Monte Carlo dispersion analysis is performed to determine the robustness of the vehicle configuration to errors in entry conditions and vehicle parameters. The parameters in Table 2 are randomly varied assuming normal distribution. The variations tested are similar to those used for the analysis of MSL by Striepe et al.[21] The atmospheric data is also varied in every iteration by using different datasets from MarsGRAM 2005. A MATLAB Simulink model implementing a full simulation of the descent trajectory is used for the Monte Carlo analysis. The guidance algorithm described in Chapter VI and Appendix C-D is also incorporated into this system. The dispersions are obtained by running 2000 iterations, starting at the entry interface and terminating at a velocity of 600 m/s which corresponds to Powered Descent Initiation (PDI).

The results from the Monte-Carlo analysis are show in Figures 13 and 14. Figure 13 shows the spread in the position of the spacecraft at PDI, in essence giving a positional error "ellipse" at PDI. This is not at a constant altitude since the termination of guidance is determined by velocity and depending on the dispersion of parameters there is a slight variation in the PDI altitude. The 99% footprint at PDI is found to be around 20 km along the downrange direction and less than 0.6 km along the crossrange direction. However, if we consider only 95% of the points, the footprint is further reduced to 10 km x 0.4 km. This is comparable, if not better than what previous Mars missions have accomplished and allows for pin-point landing during the powered-descent phase.

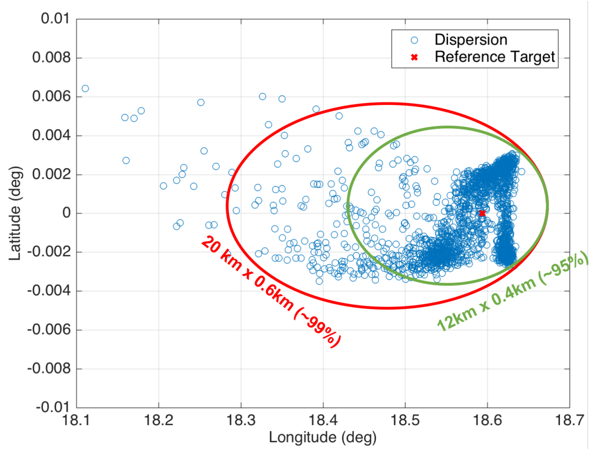

Figure 13: Position Error at PDI

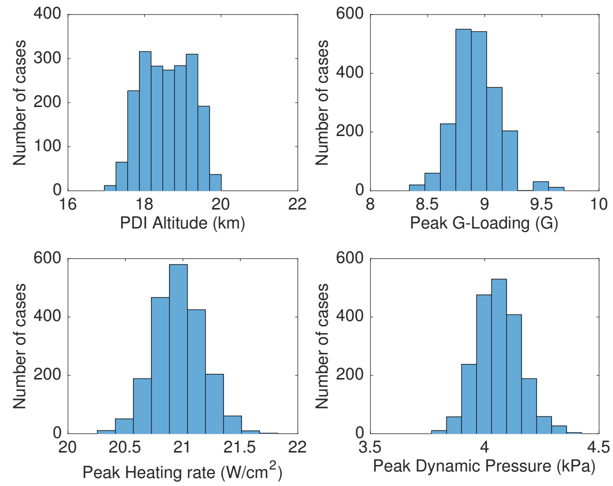

Figure 14: Sample Monte-Carlo Results at PDI

The variation in PDI altitude along with variations in peak heating rate, G-loading, and peak dynamic pressure are shown in Figure 14. The heating rate was computed using Sutton and Graves equation from Eq. 1.[16] The G-loading, though on the higher side of human endurance, is dependent on the reference trajectory. A very simple reference trajectory with two constant bank angle phases were chosen as described in Chapter VI, due to time constraints. A better trajectory with lower G-loading can be found using optimization and the guidance algorithm is capable of following it. The mean PDI altitude of around 18.5km also helps increase the reachability of the vehicle configuration to higher-altitude landing sites, though this would be dependent on the performance of the propulsion system used for landing.

Table 2: Monte-Carlo Parameters and Variations[21]

Variable	Nominal	Variation	Units	Type
Entry flight-path angle	-12.0°	0.6	°	Gaussian 3-sigma
C_L multiplier	1.0	0.1		Gaussian 3-sigma
C_D multiplier	1.0	0.1		Gaussian 3-sigma
C_Y multiplier	1.0	0.1		Gaussian 3-sigma

X. Challenges, Future Work, and Cost

A. Challenges

The main challenge of this project is the proper prediction of the motion of the entry body. Due to numerous design parameters, each dealing with a different technical aspect of the final shape of the inflatable system, there is a compromise between aero-thermodynamic, mechanical, and controllability aspects.

One of the main challenges stems from the aerodynamic nature of entry vehicles. The large Mach number causes a bow shock to form forward of the stagnation point, and staying close to the body's geometry. A potential issue with using extending flaps is that a separation bubble may form at the corner where the control surface begins, creating a shock at the upstream end of the bubble. Interactions between this shock and the bow shock may lead to shock-shock interactions that causes localized increased heating on the flap. This may lead to limitations on the flap length or maximum trim angle.

Another challenge is linked to the structure of the vehicle. From a control viewpoint, the actuators should be as powerful as possible in order to provide quicker changes; however, the maximum payload would have to decrease in order to compensate for the larger mass.

The controllability depends on all mentioned aspects. In order to achieve a high maneuverability as well as a short response time the vehicle mass distribution has to be tailored well to the control surfaces.

B. Future Work and Cost

Work to be done in the future includes:

- Development of a pin-lock mechanism designed to stop the arm from buckling when the actuator extends.
- CFD analyses to determine the flow field and temperature profile to a higher fidelity
- Trajectory optimization to bring down g-loading
- Reaction control system design analysis to maintain roll angle of the vehicle at 0^o
- Material selection for TPS and heating analysis to find temperature profile of vehicle.
- Further analysis of the actuator support to make sure it does not decrease the stability of the actuator system
- Relative environment deployment to determine the actuator dynamics and design
- Aeroelastic analyses to ensure the structural integrity and aerodynamic stability

Table 3 presents a projected timeline of the analysis of iPADDLES. The design of the vehicle is guided by the mission it will fly, and therefore the first aspects that will be examined in detail are the reference trajectory and aerodynamics of the vehicle. From this, important requirements can be drawn for the actuator-flap system. After a design review, each component of iPADDLES will be looked at in detail and changed if necessary. Some of this work is planned to take place in the Summer of 2016.

Table 3: Project Timeline

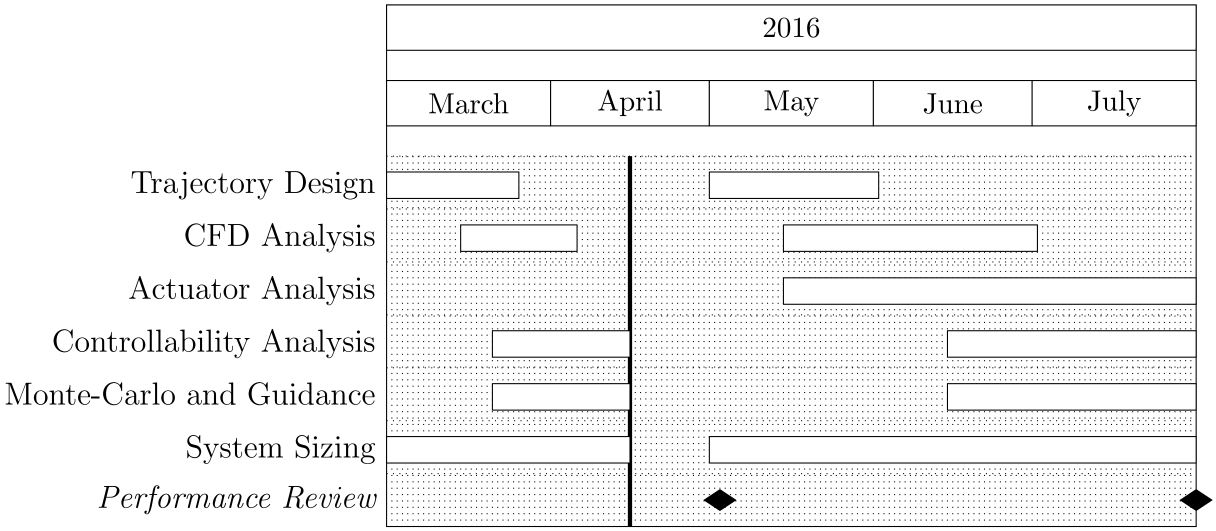

XI. Conclusion

The benefits of iPADDLES are seen in three aspects: simplicity, packaging, and control. Since the only system added to the already lightweight stacked toroid HIAD design is a lightweight actuator system, iPADDLES maintains this advantage. The same argument can be made for iPADDLES's packaging ability. Based off of IRVE 2, IRVE 3, and the HEART program, it has been proved that a stacked toroid can be packaged and deployed. It can be assumed the actuator system can be packaged easily as well since it takes up only a fraction of the overall volume, however, the deployment will need to be tested multiple times in order to determine the success of the design.

The actuated flap design has a large advantage for controllability. Placing multiple actuators along the outer radius allows for bounded control in multiple directions and a range of magnitudes. In addition, placing the control surfaces far away from the center of gravity allows for longer moment arms to aid in adjusting the AoA. Flaps placed symmetrically around the circumference of the toroid with 90° of separation allows for independent control of sideslip and AoA. With iPADDLES, S-turns do not need to be used for guidance, allowing for more precision in crossrange.

iPADDLES can achieve an L/D of about 0.5, and can modulate between zero and that maximum while also controlling the drag area and therefore deceleration force. iPADDLES is able to achieve this while staying withing the diameter constraints of 15 - 20 m, and using a payload mass of 50 metric tons. An important aspect to note is that while increasing L/D, drag is increased alongside lift. Also, the change in trim AoA and trim sideslip angle can be achieved extremely fast with the electro-mechanical actuator.

Appendices

A. Nomenclature

A_{ref}	Reference Area of the Vehicle
C_L	Lift Coefficient
C_D	Drag Coefficient
D	Drag
g	Acceleration due to Gravity
h	Altitude from the Ground
H	Scale Height
K	Proportionality Constant for Modified Newtonian Impact Theory
l	Reference Length for Moments
L	Lift
m	Mass
R	Radius
S	Downrange Distance
t	Time
u	Control Variable
v	Velocity
$\vec{X}$	State Vector
α	AoA
β	Angle of Sideslip
γ	Vehicle Flight Path angle
δ	Sphere-Cone Deflection Angle
λ	Co-state
ω	Flap Deflection Angle or Apollo Guidance Parameter
ϕ	Angular Coordinate Defining Position on Circumference or Latitude
θ	Angular Coordinate Defining Position on Vehicle Cross-Section or Longitude
ψ	Heading Angle
σ	Bank Angle
η	Angle between Inwards Surface Normal and Free-Stream Velocity
ρ	Density
μ	Gravitational Parameter
Subscripts	
b	Base
i	Flap Number
n	Nose
m	Mars
w	Wind Frame
x	Component in X-direction
y	Component in Y-direction
z	Component in Z-direction

B. Analysis of Aerodynamics

The aerodynamic properties are studied by employing panel methods and Newtonian impact theory. In Newtonian flow theory, the fluid is assumed to transfer all of its normal momentum to the surface of the vehicle and retain all of its tangential momentum. Consequently, the non-dimensional pressure coefficient, C_p, at any point on the surface of the vehicle is given by:

$$C_p = 2\sin(\eta)^2 \tag{2}$$

where η is the angle between the surface and the freestream vector.[22] Moreover, the pressure exerted by the fluid on the surface that is not directly exposed to the flow is assumed to be equal to the free stream pressure. Therefore, in the shadowed region, $C_p = 0$. In the panel method,[23] the vehicle is represented by a finite number of flat panels. The force and moment on each panel is computed and summed up. The flaps are modeled as flat plates. To determine the maximum AoA that the vehicle can achieve, two of the four flaps are deployed.

In order to achieve a higher level of accuracy, an analytical method is applied by integrating Eq. 2 over the entire windward surface. The convention follows the Clark and Trimmer report, where the normal vector is the inward facing vector.[24] These equations are integrated for any AoA, yaw angle, and bank angle. The Newtonian impact theory allows for aerodynamic coefficients to be added up together to create an overall vehicle coefficient. For this vehicle, the base sphere-cone was modeled as a spherical section and a wholly-revolved frustum cone, while the flaps themselves are modeled as partially-revolved frustum cones, with each flap being independent of the others.

To account for any shadowing that may occur, a line of action is calculated for where the shadowed portion of the vehicle surface begins for each of the elementary shapes. For each of the shapes, the angle ϕ_0 is calculated as the angle that the shadowed portion started at.

$$\phi_0 = -\arcsin\frac{\tan\delta}{\tan\alpha'} \tag{3}$$

where α' is the combined AoA and yaw angle.

$$\alpha' = \arccos\left(\cos\alpha\cos\beta\right) \tag{4}$$

To account for the varying location of the shadowing, ϕ_0 is calculated using with the following, with C determining the quadrant that the shadowing appears in.

$$\phi_0 = \pm\arccos\frac{\tan\delta}{\tan\alpha} + C + \mp\arccos\frac{\tan\delta}{\tan\alpha'} \tag{5}$$

Any shadowing occurring on the flaps is calculated using the same equation, except with δ replaced with the flap angle, ω_i.

A. Equations for Aerodynamic Coefficients

Using modified Newtonian impact theory, the pressure coefficient can be integrated over the surfaces to calculate the normal, axial, and side forces. These, in turn, are used to calculate drag, lift, moment, roll, and yaw coefficients.

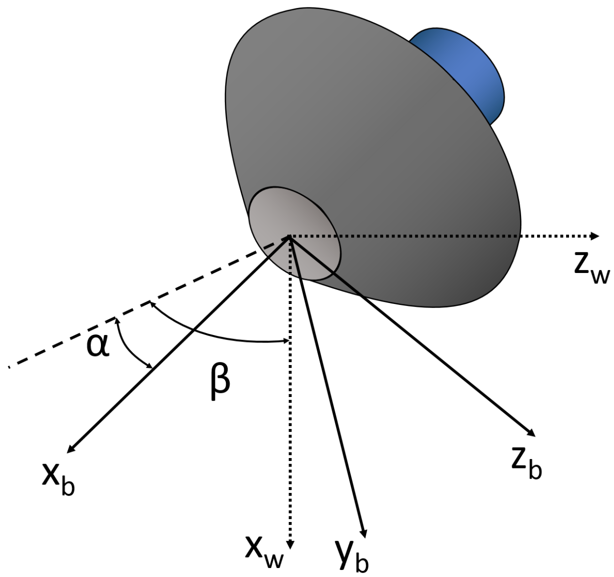

Figure 15: Representation of the sideslip and AoAs. The y_w axis is orthogonal to the x_w and z_w axes, pointing down.

$$C_N = -\frac{K}{A_{ref}} \iint_A \cos^2 \eta (\hat{e_z} \cdot \hat{n}) dA \tag{6a}$$

$$C_A = -\frac{K}{A_{ref}} \iint_A \cos^2 \eta (\hat{e_x} \cdot \hat{n}) dA \tag{6b}$$

$$C_Y = -\frac{K}{A_{ref}} \iint_A \cos^2 \eta (\hat{e_y} \cdot \hat{n}) dA \tag{6c}$$

$$C_m = \frac{K}{A_{ref} l} \left[\iint_A x \cos^2 \eta (\hat{e_z} \cdot \hat{n}) dA - \iint_A z \cos^2 \eta (\hat{e_x} \cdot \hat{n}) dA \right] \tag{6d}$$

$$C_n = \frac{K}{A_{ref} l} \left[\iint_A x \cos^2 \eta (\hat{e_y} \cdot \hat{n}) dA - \iint_A y \cos^2 \eta (\hat{e_x} \cdot \hat{n}) dA \right] \tag{6e}$$

$$C_l = \frac{K}{A_{ref} l} \left[\iint_A y \cos^2 \eta (\hat{e_z} \cdot \hat{n}) dA - \iint_A z \cos^2 \eta (\hat{e_y} \cdot \hat{n}) dA \right] \tag{6f}$$

For the conical section and flaps

$$
\begin{aligned}
C_N =&\frac{K}{A_{ref}}\Big[-\cos^2\alpha\cos^2\beta\sin^2\omega\cos\phi-\cos\alpha\cos\beta\sin\omega\sin\beta\cos\omega\cos^2\phi+\\
&\cos\alpha\cos^2\beta\sin\omega\sin\alpha\cos\omega(\phi-\sin\phi\cos\phi)+\frac{2}{3}\sin\beta\cos^2\omega\sin\alpha\cos\beta\sin^3\phi-\\
&\frac{1}{3}\sin^2\beta\cos^2\omega\cos^3\phi+\frac{1}{12}\sin^2\alpha\cos^2\beta\cos^2\omega(\cos 3\phi-9\cos\phi)\Big]|_{\phi_1}^{\phi_2}
\end{aligned}
\tag{7a}
$$

$$
\begin{aligned}
C_A =&\frac{K}{A_{ref}}\Big[\cos^2\alpha\cos^2\beta\sin^3\omega\phi+2\cos\alpha\cos\beta\sin^2\omega\sin\beta\cos\omega\sin\phi-\\
&2\cos\alpha\cos^2\beta\sin^2\omega\sin\alpha\cos\omega\cos\phi-\sin\beta\cos^2\omega\sin\alpha\cos\beta\sin\omega\cos^2\phi+\\
&\frac{1}{2}\sin^2\beta\cos^2\omega\sin\omega(\phi+\sin\phi\cos\phi)+\\
&\frac{1}{2}\sin^2\alpha\cos^2\beta\cos^2\omega\sin\omega(\phi-\sin\phi\cos\phi)\Big]|_{\phi_1}^{\phi_2}
\end{aligned}
\tag{7b}
$$

$$
\begin{aligned}
C_Y =&\frac{K}{A_{ref}}\Big[\cos^2\alpha\cos^2\beta\sin\omega\sin\phi+\cos\alpha\cos\beta\sin\omega\sin\beta\cos\omega(\phi+\sin\phi\cos\phi)-\\
&\cos\alpha\cos^2\beta\sin\alpha\cos\omega\cos^2\phi+\frac{1}{12}\sin^2\beta\cos^2\omega(9\sin\phi+\sin 3\phi)-\\
&\frac{2}{3}\sin\beta\cos^2\omega\sin\alpha\cos\beta\cos^3\phi+\frac{1}{3}\sin^2\alpha\cos^2\beta\cos^2\omega\Big]|_{\phi_1}^{\phi_2}
\end{aligned}
\tag{7c}
$$

For the spherical section

$$
\begin{aligned}
C_N =&\frac{K}{A_{ref}}\Big[\frac{1}{32}\cos^2\beta\cos\alpha^2\cos\phi(\sin 4\theta-4\theta)+\frac{1}{4}\cos^2\beta\cos\alpha\sin\alpha\sin^4\theta(\phi-\sin\phi\cos\phi)-\\
&\frac{1}{4}\cos\beta\cos\alpha\sin\beta\cos^2\phi\sin^4\theta+\frac{1}{32}(12\theta-8\sin 2\theta+\sin 4\theta)\\
&(\frac{2}{3}\cos\beta\sin\beta\sin\alpha\sin^3\phi+\frac{1}{12}\cos^2\beta\sin^2\alpha(\cos 3\phi-9\cos\phi)-\frac{1}{3}\sin^2\beta\cos^3\phi]|_{\phi_1}^{\phi_2}|_{\theta_1}^{\theta_2}
\end{aligned}
\tag{8a}
$$

$$
\begin{aligned}
C_A =&\frac{K}{A_{ref}}\Big\{-\frac{1}{4}\cos^2\beta\cos^2\alpha\phi\cos^4\theta-\frac{1}{16}(4\theta-\sin^4\theta)\cos^2\beta\cos\alpha\sin\alpha\cos\phi+\\
&\frac{1}{16}\cos\beta\cos\alpha\sin\beta\sin\phi(4\theta-\sin^4\theta)+\frac{1}{4}\sin^4\theta\Big[-\cos\beta\sin\alpha\sin\beta\cos^2\phi+\\
&\frac{1}{2}\cos^2\beta\sin^2\alpha(\phi-\sin\phi\cos\phi)+\frac{1}{2}\sin^2\beta(\phi+\sin\phi\cos\phi)\Big]\Big\}|_{\phi_1}^{\phi_2}|_{\theta_1}^{\theta_2}
\end{aligned}
\tag{8b}
$$

$$
\begin{aligned}
C_Y =&\frac{K}{A_{ref}}\Big\{\frac{1}{32}\cos^2\beta\cos^2\alpha\sin\phi\Big[4\theta-\sin^4\theta\Big]-\frac{1}{4}\cos^2\beta\cos\alpha\sin\alpha\cos^2\phi\sin^4\theta+\\
&\frac{1}{4}\cos\beta\cos\alpha\sin\beta\Big[\phi+\sin\phi\cos\phi\Big]\sin^4\theta+\frac{1}{32}\Big[12\theta-8\sin 2\theta+\sin 4\theta\Big]\\
&\Big[-\frac{2}{3}\cos\beta\sin\beta\sin\alpha\cos^3\phi+\frac{1}{3}\cos\beta\sin^2\alpha\sin^3\phi+\\
&\frac{1}{12}\sin^2\beta(9\sin\phi+\sin 3\phi)\Big]\Big\}|_{\phi_1}^{\phi_2}|_{\theta_1}^{\theta_2}
\end{aligned}
\tag{8c}
$$

B. Additional Plots from Max L/D Configuration

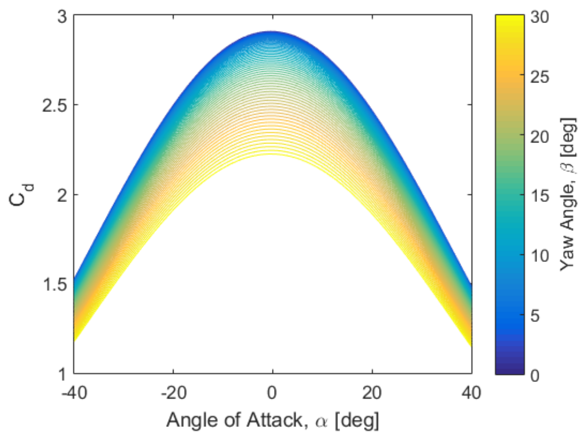

Figure 16: Drag coefficient as a function of AoA. The maximum occurs at no sideslip or AoA, at approximately 2.9.

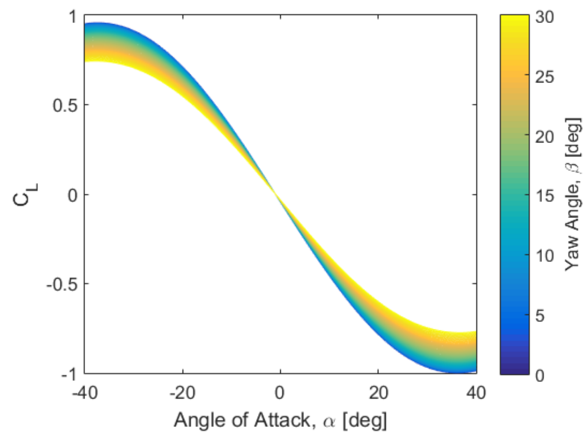

Figure 17: Lift coefficient as a function of AoA. The maximum occurs at no sideslip angle and at an AoA of about 38°. The maximum c_L is about 1.0.

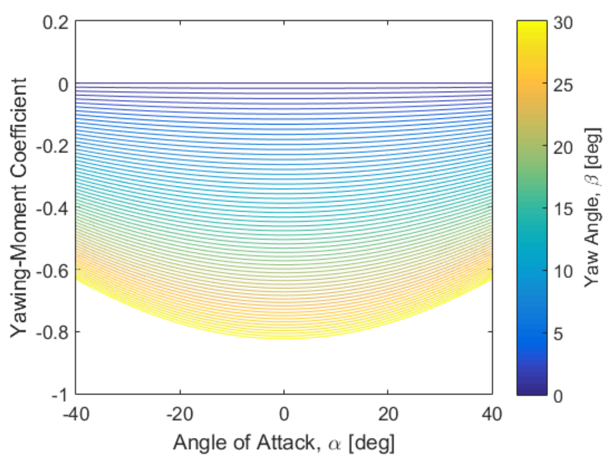

Figure 18: Sideforce coefficient as a function of AoA. As expected, the forces from both sides are equal in magnitude, but opposite in direction due to the body's symmetry.

C. Sideslip Augmented Apollo Guidance Algorithm: Downrange Channel

This section describes the downrange channel of the original Apollo reentry guidance algorithm,[10] and the modifications made to it to accommodate the new control strategy designed for the HIAD vehicle. The planar equations of motion for atmospheric entry flight can be approximated as:

$$\dot{S} = v\cos\gamma \tag{9a}$$

$$\dot{v} = -\left(\frac{D}{m} + g\sin\gamma\right) \tag{9b}$$

$$\dot{\gamma} = \frac{1}{mv}L\cos\sigma + \left(\frac{v}{R_m + h} - \frac{g}{v}\right)\cos\gamma \tag{9c}$$

$$\dot{h} = v\sin\gamma \tag{9d}$$

where

$$D = \frac{1}{2}\rho v^2 C_D A_{ref} \tag{10a}$$

$$L = \frac{1}{2}\rho v^2 C_L A_{ref} \tag{10b}$$

$$\rho = \rho_0 e^{-\frac{h}{H}} \tag{10c}$$

$$g = \frac{\mu}{(R_m + h)^2} \tag{10d}$$

These equations of motion can be represented as:

$$\dot{\vec{X}} = f(\vec{X}, \sigma, t) \tag{11}$$

The reference planar trajectory is generated from these planar equations of motion.

A costate vector is defined as follows:

$$\lambda = \Big[[\lambda_S \quad \lambda_v \quad \lambda_\gamma \quad \lambda_h]\Big]^T \tag{12}$$

The dynamics for the costate vector can be derived to be:

$$\dot{\lambda}^T = -\lambda^T \frac{\partial f}{\partial X} \tag{13}$$

The costate variables are determined by reverse-propagating the costate dynamics using the following final condition:

$$\lambda^T(t_f) = \frac{\partial f}{\partial X_f} = \Big[[1 \quad 0 \quad \csc^2\gamma_f {h_f}^* \quad -\cot\gamma_f]\Big] \tag{14}$$

A parameter ω is defined as:

$$\omega = \int_{t_0}^{t_f} \frac{\partial f}{\partial u}^T \lambda dt \tag{15}$$

Consequently, the differential equation for ω can be computed from Leibniz rule as:

$$\dot{\omega} = -\frac{\partial f^T}{\partial \sigma} \tag{16}$$

ω can be computed along the reference trajectory by reverse-propagating $\dot{\omega}$ with the final condition $\omega(t_f) = 0$.

In the guidance algorithm, velocity is used as the independent variable because it is not important to reach the terminal downrange at the reference final time, but it is important to reach target at a velocity that is close to the final velocity along the reference. Consequently, the change in bank angle from the reference is computed by the guidance algorithm as:

$$\delta\sigma = \frac{-\lambda_S^*(v_0)\delta S(v0) - \frac{\lambda_\gamma^*(v_0)}{v_0 cos\gamma^*(v_0)}\delta\dot{h}(v_0) + \frac{mH\lambda_h^*(v_0)}{D^*(v_0)}\frac{D(v_0)}{m}}{\omega^*(v_0)} \tag{17}$$

The commanded bank angle is given by:

$$u_{command} = u^* = \delta u \tag{18}$$

The sign of $\sigma_{command}$ is computed by the crossrange channel. The perturbation variables are computed as:

$$\delta S(v_0) = S(v_0) - S^*(v_0) \tag{19a}$$

$$\delta\dot{h}(v_0) = \dot{h}(v_0) - \dot{h}^*(v_0) \tag{19b}$$

$$\delta D(v_0) = D(v_0) - D^*(v_0) \tag{19c}$$

The superscript $*$ indicates that the quantity is computed along the reference trajectory. The reference quantities are calculated offline and stored in the onboard computer before atmospheric entry.

Since the HIAD vehicle introduces an α and a β in response to a bank command by suitably deflecting the tabs, the drag coefficient varies. It was found that in general, the lift coefficient increased and the drag coefficient reduced by a small amount. As a result, if no modifications are made to the algorithm, the vehicle will overshoot the target. Therefore, a correction factor was added to the sensed drag acceleration to make the algorithm think that the vehicle is encountering less drag. This will force the algorithm to command a steeper bank angle (resulting in less vertical lift), and hence, reduce the overshoot. This correction factor is a design parameter that needs to be tuned to achieve satisfactory targeting performance. For this HIAD vehicle, the correction factor was found to be 0.8. Consequently, drag error gets modified as:

$$\delta D(v_0) = 0.8D(v_0) - D^*(v_0) \tag{20}$$

D. Sideslip Augmented Apollo Guidance Algorithm: Crossrange Channel

In the original Apollo guidance algorithm,[10] the crossrange channel commands a roll reversal whenever the crossrange error hits a deadband. For the HIAD vehicle, the algorithm was modified to command a roll reversal when the heading error hits a deadband. The algorithm was also modified to calculate the great circle range to the target and report it to the downrange channel to compute the equivalent downrange along the planar reference trajectory.

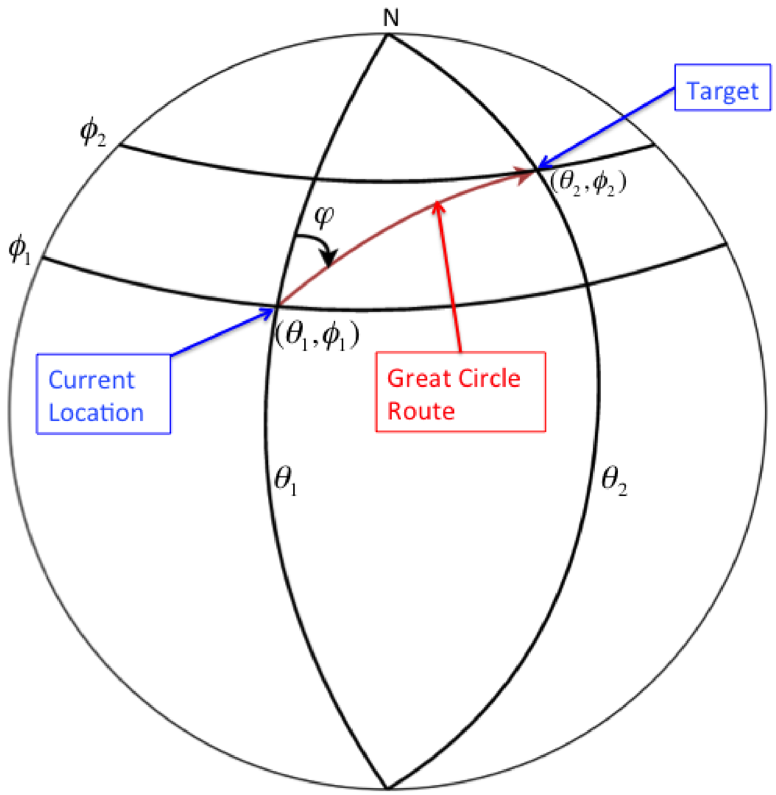

Figure 19: Illustration of computation of great circle route to the target from the current location

From the present latitude and longitude coordinates, the great circle route is computed to the desired target (Figure 19). The heading angle to the target is:

$$\psi = tan^{-1}\left(\frac{sin(\theta_2 - \theta_1)}{cos\phi_1 tan\phi_2 - sin\phi_1 cos(\theta_2 - \theta_1)}\right) \tag{21}$$

The heading error is computed as:

$$\delta\psi = \psi_{(Current)} - \psi \tag{22}$$

When the magnitude of $\delta\psi$ exceeds 1.5°., a roll reversal is commanded. The initial direction of bank is chosen such that it reduces the heading error.

From the computed bank angle command, the equivalent angle-of-attack and sideslip angles are resolved as shown in Figure 20 and computed as follows:

$$\alpha = \sin^{-1}\left(sin\left(\alpha_{Apollo}\right) cos\left(\sigma_{Apollo}\right)\right) \tag{23a}$$

$$\beta = sgn\left(sin\left(\sigma_{Apollo}\right)\right) cos^{-1}\left(\frac{cos\left(\alpha_{Apollo}\right)}{cos\left(\alpha\right)}\right) \tag{23b}$$

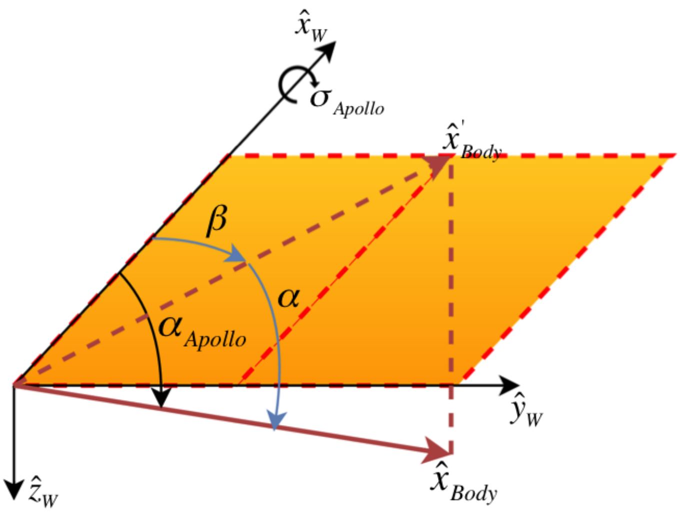

Figure 20: Illustration of resolution of bank-angle into AoA and side-slip sequence

The distance to the target is computed as:

$$S_{(To\ go)} = R_m\ cos^{-1}\left(sin\phi_1 sin\phi_2 + cos\phi_1 cos\phi_2 cos\left(\theta_2 - \theta_1\right)\right) \tag{24}$$

$S_{(TO\ go)}$ is supplied to the downrange channel to where it is used to compute the representative downrange along the planar trajectory as follows:

$$S = S_f - S_{(To\ go)} \tag{25}$$

where S_f is the final downrange along the planar reference trajectory. This S will be used as the $S(v_0)$ in equation 19a.

E. Trajectory Profile Plots

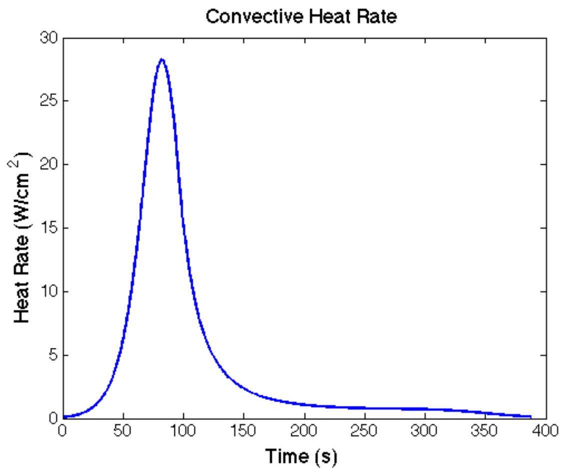

Figure 21: Convective heat rate encountered by vehicle through the hypersonic reference trajectory phase.

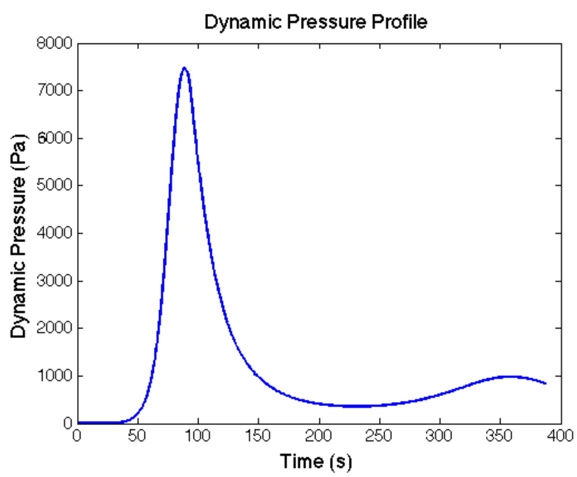

Figure 22: Dynamic pressure profile along vehicle reference trajectory.

F. Inflatable Balloon Control System

Another explored architecture for the flap system that was considered during the design study is the so-called **Inflatable Balloon Control System**. The basic idea is to use additional inflatable toroids being pressurized by an external gas tank to deflect the control flaps. Fast opening and closing valves guarantee a short response characteristic. Numerous technical concerns led finally to a withdrawal of this concept though including gas release locations that would not undermine the capability of the TPS to perform its job. Figure 23 illustrates its principle technical functionality.

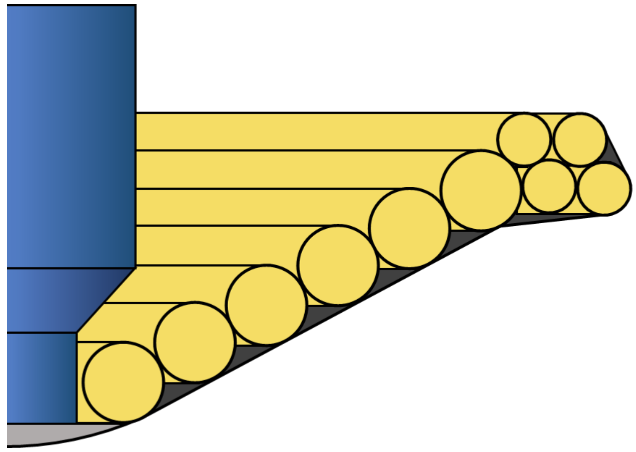

Figure 23: Cut-away view of the inflatable tab system. Instead of a mechanical system, the tabs will deflect into the flow by inflating the three bladders in a triangle formation. When deflated, they will sit flush along the 70 sphere cone half angle.

This system is appealing due to an appreciable low amount of mechanical components resulting in a reduced structure mass, easier packaging for launch, and increased technical reliability. The continued use of inflatables as controls offers the benefit of minimizing systems needed to go through testing. However, the finite amount of gas in the tanks limited the amount of maneuvers that could be performed, as well as quickly reducing the number of trajectories that may be used. Additionally, the geometric size of all four flaps requires an extremely high operating pressure, which consequently increases both the volume and mass of the pressurized tank. At the end of the design study it was not clear if such a tank is realistic, from a technical as well as financial perspective.

References

[1]A. M. D. Cianciolo, J. L. Davis, D. R. Komar, M. M. Munk, J. A. Samareh, J. A. Williams-Byrd, T. A. Zang, R. W. Powell, J. D. Shidner, D. O. Stanley *et al.*, *Entry, Descent and Landing Systems Analysis Study: Phase 1 Report.* National Aeronautics and Space Administration, Langley Research Center, 2010.

[2]B. P. Smith, C. L. Tanner, M. Mahzari, I. G. Clark, R. D. Braun, and F. M. Cheatwood, "A historical review of inflatable aerodynamic decelerator technology development," in *Aerospace Conference, 2010 IEEE.* IEEE, 2010, pp. 1–18.

[3]R. A. Dillman, S. J. Hughes, R. J. Bodkin, D. M. Bose, J. D. Corso, and F. N. Cheatwood, "Flight performance of the inflatable reentry vehicle experiment ii," https://solarsystem.nasa.gov/docs/p484.pdf, accessed: 2016-03-03.

[4]B. R. J. D. C. J. Dillman R. A., Hughes S. J. and C. F. M., "Flight performance of the inflatable reentry vehicle experiment 3," 2011.

[5]R. Dillman, J. DiNonno, R. Bodkin, V. Gsell, N. Miller, A. Olds, and W. Bruce, "Flight performance of the inflatable reentry vehicle experiment 3," in *10th International Planetary Probe Workshop*, 2013, accessed: 2016-03-03.

[6]A. Mazaheri, "High-energy atmospheric reentry test aerothermodynamic analysis," *Journal of Spacecraft and Rockets*, vol. 50, no. 2, pp. 270–281, 2013.

[7]H. Wright, A. Cutright, J. Corliss, W. Bruce, D. Trombetta, A. Mazaheri, M. Coleman, A. Olds, and S. Hancock, "Heart flight test overview," in *9th International Planetary Probe Workshop*, 2012, pp. 16–22.

[8]B. P. Harper and R. D. Braun, "Asymmetrically stacked tori hypersonic inflatable aerodynamic decelerator design study for mars entry," in *AIAA Atmospheric Flight Mechanics Conference*, 2014, p. 1095.

[9]J. S. Green, B. Dunn, and R. Lindberg, "Morphing hypersonic inflatable aerodynamic decelerator," in *AIAA Aerodynamic Decelerator Systems (ADS) Conference*, 2013, p. 1256.

[10]R. Morth, "Reentry guidance for apollo," *MIT/IL R-532*, vol. I, 1966.

[11]T. L. Motion, "Ect-series precision linear actuators," www.thomsonlinear.com/website/com/eng/products/actuators/ect_series.php, accessed: 2016-03-03.

[12]D. Verhoeven and F. D. Coster, "Electro-mechanical actuators (emas) for space applications," http://www.esmats.eu/esmatspapers/pastpapers/pdfs/2013/verhoeven.pdf, accessed: 2016-03-03.

[13]M. Kerr, R. Haya, L. Peñín, G. De Zaiacomo, D. Mostaza, and V. Marco, "Ixv re-entry guidance, control & drs triggering: Algorithm design and assessment," in *AIAA Guidance, Navigation, and Control Conference*, 2012, p. 4841.

[14]R. Dillman, "Flight performance of the inflatable reentry vehicle experiment ii," in *7th International Planetary Probe Workshop*, 2010, accessed: 2016-03-03.

[15]R. Dillman, N. Cheatwood, S. Hughes, J. Del Corso, R. J. Bodkin, and A. Olds, "Planned flight of the inflatable reentry vehicle experiment 3 (irve-3)," in *8th International Planetary Probe Workshop*, 2011, accessed: 2016-03-03.

[16]K. Sutton and R. A. Graves Jr, "A general stagnation-point convective heating equation for arbitrary gas mixtures," 1971.

[17]D. A. Spencer, R. C. Blanchard, R. D. Braun, P. H. Kallemeyn, and S. W. Thurman, "Mars pathfinder entry, descent, and landing reconstruction," *Journal of Spacecraft and Rockets*, vol. 36, no. 3, pp. 357–366, 1999.

[18]D. K. Litton, D. M. Bose, F. Cheatwood, S. Hughes, H. S. Wright, M. C. Lindell, S. D. Derry, and A. Olds, "Inflatable re-entry vehicle experiment (irve)-4 overview," in *21st AIAA Aerodynamic Decelerator Systems Technology Conference and Seminar*, 2011, p. 2580.

[19]Y. Gibbs, "Nasa armstrong fact sheet: X-38 prototype crew return vehicle," https://www.nasa.gov/centers/armstrong/news/FactSheets/FS-038-DFRC.html, accessed: 2016-02-27.

[20]D. W. Way, R. W. Powel, A. Chen, A. D. Steltzner, P. D. Burkhart, G. F. Mendeck *et al.*, "Mars science laboratory: Entry, descent, and landing system performance," in *Aerospace Conference, 2007 IEEE*. IEEE, 2007, pp. 1–19.

[21]S. A. Striepe, D. Way, A. Dwyer, and J. Balaram, "Mars science laboratory simulations for entry, descent, and landing," *Journal of Spacecraft and Rockets*, vol. 43, no. 2, pp. 311–323, 2006.

[22]J. D. Anderson, *Hypersonic and High Temperature Gas Dynamics*. AIAA, 2000.

[23]M. J. Grant and R. D. Braun, "Analytic hypersonic aerodynamics for conceptual design of entry vehicles," in *48th AIAA Aerospace Sciences Meeting Including the New Horizons Forum and Aerospace Exposition*, 2010, pp. 2010–1212.

[24]E. L. Clark and L. L. Trimmer, "Equations and chart for the evaluation of the hypersonic aerodynamic characteristics of lifting configurations by the newtonian theory," 1964.